

# FRI Sensing: Retrieving the Trajectory of a Mobile Sensor From Its Temporal Samples

Ruiming Guo<sup>✉</sup> and Thierry Blu<sup>✉</sup>, *Fellow, IEEE*

**Abstract**—In this article, contrary to current research trend which consists of fusing (big) data from many different sensors, we focus on one-dimensional samples collected by a unique mobile sensor (e.g., temperature, pressure, magnetic field, etc.), *without* explicit positioning information (such as GPS). We demonstrate that this stream of 1D data contains valuable 2D geometric information that can be unveiled by adequate processing—using a high-accuracy Finite Rate of Innovation (FRI) algorithm: “FRI Sensing”. Our key finding is that, despite the absence of any position information, the basic sequence of 1D sensor samples makes it possible to reconstruct the sampling trajectory (up to an affine transformation), and then the image that represents the physical field that has been sampled. We state the FRI Sensing sampling theorem and the hypotheses needed for this trajectory and image reconstruction to be successful. The proof of our theorem is constructive and leads to a very efficient and robust algorithm, which we validate in various conditions. Moreover, although we essentially model the images as finite sums of 2D sinusoids, we also observe that our algorithm works accurately for real textured images.

**Index Terms**—Mobile sensing, finite rate of innovation, sampling theory, curve estimation.

## I. INTRODUCTION

THE wide availability of cheap sensors of various kinds (inertia, magnetic field, light, temperature, pressure, chemicals etc.) makes it possible to develop new applications. An important problem is sensor data fusion. For example, it is necessary to combine temperature, humidity, atmospheric pressure and wind velocity information together to predict future weather trends [1], [2], [3].

In practical applications, people usually obtain the position information through GPS (Global Position System) using multilateration techniques. However, GPS positioning is not feasible and available in many scenarios due to environmental limitations. For example, in outdoor applications, complex terrains like hills, trees, or caves may block the GPS signal and weaken the positioning signal strength [4] as shown in Figs. 1(b) and 1(d). In submarine detection, people often choose sound waves instead of radio waves because they are significantly less attenuated underwater [5] as shown in Fig. 1(c). Besides, installing a GPS

Manuscript received December 10, 2019; revised June 23, 2020; accepted August 29, 2020. Date of publication September 11, 2020; date of current version October 6, 2020. The associate editor coordinating the review of this manuscript and approving it for publication was Dr. Gwo Giun Lee. (*Corresponding author:* Ruiming Guo.)

The authors are with the Department of Electronic Engineering, The Chinese University of Hong Kong, 999077, Hong Kong (e-mail: 1155100873@link.cuhk.edu.hk; thierry.blu@m4x.org).

Digital Object Identifier 10.1109/TSP.2020.3022816

receiver on each sensor device is cost and energy prohibitive in many applications. For example, people often need to install bulky tags onto the marked animals [6] which run out of energy quickly in wild animal tracking in Fig. 1(a). Moreover, the patch sensors mounted on the insects and birds are of small size in order to reduce the influence on their normal activities which further limits the battery capability of GPS devices.

The field of mobile sensor localization has been studied in many research communities. Triangulation methods [7], [8] are one of the most popular. These methods estimate the mobile sensor positions by measuring angles or distances to a number of beacon nodes, utilizing models that characterize how acoustic or radio signals propagate in space. However, these methods require dense deployment of sensor nodes, which is unavailable in many applications, such as undersea detection in Fig. 1(c) and remote monitoring in Fig. 2(f). An alternative solution is trajectory mapping/matching which requires prior measurement of a signal-strength map of the coverage area [9], [10], [11]. Then, by matching the signal-strength signature/fingerprints within this map, the position of the mobile sensor can be retrieved. However, the prior knowledge of the 2D physical field is required which is infeasible in a number of scenarios. For example, in SLAM (Simultaneous Localization And Mapping) applications, like planetary navigation [12] and mine exploration [13], the unknown physical environment makes it impossible to pre-construct this signal-strength map.

In this article, we demonstrate that the temporal samples of a (non-positioning) sensor can be processed to reveal 2D positioning information. This processing is based on the local approximation of these data as sums of sinusoids, which can be very accurately estimated using a Finite Rate of Innovation algorithm (FRI)—“FRI Sensing” [14]. The methods that we use (typ., FRI) are reminiscent of the ones used for room shape identification [15], [16] or more generally source localization from physical fields that satisfy potential/diffusion/propagation equations [17]. An essential difference in the current article is that our data do not contain any obvious geometric clues.<sup>1</sup>

For simplicity, we will limit ourselves to the 2D case in the article. Specifically, our setting is as follows: A (non-positioning) mobile sensor samples a 2D physical field along some (unknown) trajectory. After the sampling process, we obtain the 1D temporal sensor data and what we want to achieve is the reconstruction of the sampling curve (trajectory) and then, the

<sup>1</sup>All figures in Fig. 1 and Fig. 2 are randomly selected on Google Image: <https://www.google.com/imghp?hl=en>

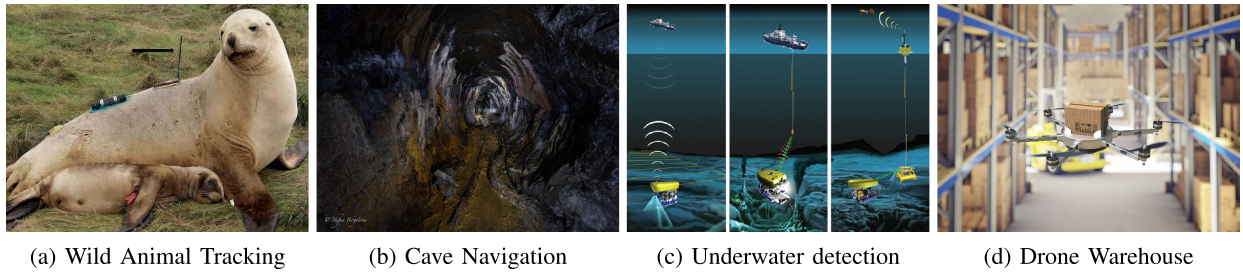


Fig. 1. **Examples when GPS is not available.** (a) Electrical power limitation (animal tracking). (b) Underground positioning. (c) Underwater positioning. (d) Indoor positioning.

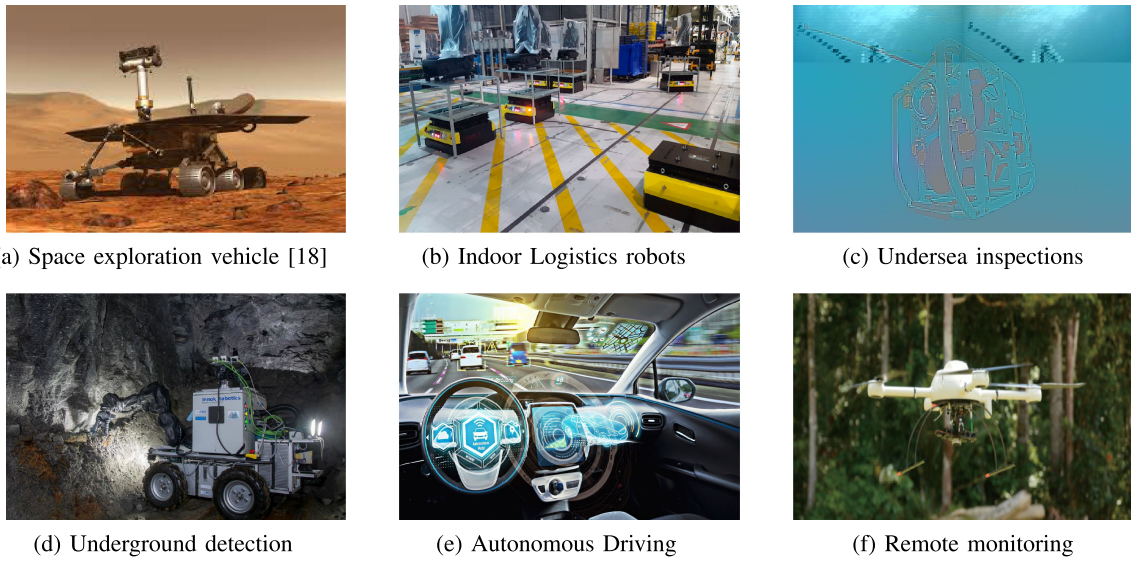


Fig. 2. **A wide range of potential applications.** (a) Space exploration car on Mars. (b) Fixed track indoor logistics robots. (c) Underwater detection robots in deep sea exploration. (d) Underground detection car in geological exploration. (e) Positioning and mapping in self-driving. (f) Remote environmental monitoring in deep forest.

2D physical field. At first glance, this program seems impossible because of the absence of multidimensional information (e.g. 2D location, velocity, etc.). However, we show that there is valuable and adequate spatial information (2D) hidden within the 1D sensor data.

Of course, for our program to be successful, both the trajectory of the sensor and the field sampled should satisfy hypotheses. We first start from the simplest case, then relax the constraints to fit the real applications more accurately. At first, we investigate the hypotheses when both the trajectory of the sensor and the sampling physical field satisfy exact sparsity conditions: the sampling trajectory is piecewise linear and the physical field is a finite sum of spatial sinusoids (global stationarity). We then relax the hypotheses on the sampling trajectory to allow some curvature and explore the corresponding reconstruction hypotheses. Moreover, even if we essentially model the image as a sum of 2D sinusoids, we still find out that our algorithm is working accurately for real textured images (see Section V).

Extracting geometric cues from a stream of 1D temporal samples is likely to be very useful, either by directly providing positioning information, or by increasing the accuracy of

other positioning methods. A potential application is SLAM (Simultaneous Localization And Mapping) in robotic navigation [18], [19], [20], e.g. in Figs. 2(b), 2(d) and 2(f). People need to construct or update a map of an unknown environment while simultaneously keeping track of an agent's location within it. However, in many application scenarios, like autonomous underwater vehicles in Fig. 2(c) and planetary rovers Fig. 2(a), GPS positioning is not available due to lack of penetration of the GPS signal. Using FRI Sensing, we could tackle the SLAM problem by collecting sensor data sampled from, e.g. the magnetic field, and then reconstruct the mobile sensor trajectory. Moreover, using sensors of different fields is likely to provide a much more accurate and robust reconstruction under available resources.

As a completely different application, the proposed method could possibly be applied to visualize arbitrary 1D signals as if they were the samples of genuine 2D images along trajectories [21], [22]; i.e., not only limited to positioning. Speech, text signals, but also many others could be considered eventually, allowing to identify visual clues and features (geometry, texture, etc) in non-visual signals, which do not necessarily have the

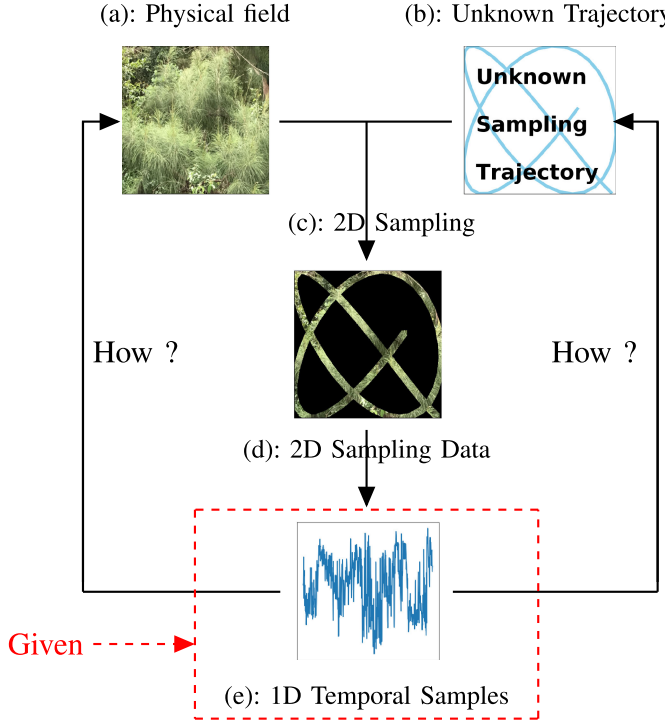


Fig. 3. “FRI sensing” is about reconstructing the 2D physical field (a) and the sampling trajectory (b) of the mobile sensor from the measured 1D time series (e).

corresponding 2D ground truth images. We speculate that this new visualization tool would reveal meaningful 2D geometries in non-geometric 1D signals, which could be exploited, e.g., for signal analysis and classification.

Reconstructing 2D image and trajectory from 1D temporal samples requires solving a number of problems:

- The first challenge is in identifying the hypotheses under which it’s possible to retrieve the sampling trajectory and image. Since the problem is severely ill-posed in the absence of 2D position information, achieving the reconstruction from as little as 1D temporal samples requires specific hypotheses on both the sampling image and trajectory. That is to say, we need a general sampling theorem to characterize the reconstruction hypotheses on both the image and trajectory.
- The second challenge is, given certain error tolerance how to accurately retrieve the trajectory position information hidden within the 1D temporal samples.
- The third difficulty falls on the image reconstruction from 1D samples. We may convert this problem into image restoration once we retrieve the sample position through the reconstructed sampling trajectory.

## II. FRI SENSING PRINCIPLES

The problem: given a 1D signal sampled from a 2D physical field along some unknown trajectory, the goal is to retrieve the 2D trajectory and the 2D physical field. Fig. 3 gives a visual depiction of this problem.

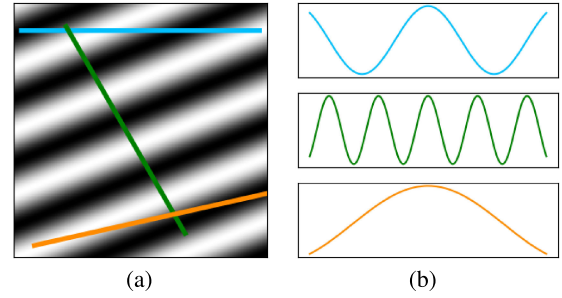


Fig. 4. Key observation: Sampling a 2D sinusoidal image along a straight line gives rise to a 1D sinusoidal signal. (a) Sampling a 2D sinusoidal image ( $K = 1$ ) along three different straight lines; (b) the resulting 1D temporal signal along these three straight lines. Obviously, the 1D frequencies of the resulting time series are closely related to the slopes of the sampling trajectories.

At first glance, it looks like this task is impossible since the problem is seriously ill-posed due to high-dimensional information loss. It seems that there is very little positioning information contained within the acquired 1D temporal samples. However, by constructing appropriate hypotheses, we show that there is rich and valuable high-dimensional information hidden within the 1D temporal samples which could be utilized to recover the 2D image and trajectory.

### A. Sampling a 2D Field Along a Curve

Let  $I(\mathbf{r})$ ,  $\mathbf{r} = [x, y]^T$  denote the image that represents the 2D physical field and  $\mathbf{r}(t) = [x(t), y(t)]^T$  denote the 2D trajectory, where  $t$  is time.

Observation: sampling a 2D sinusoidal image

$$I(\mathbf{r}) = \sum_{k=1}^K c_k e^{j\mathbf{u}_k^T \mathbf{r}} \quad (1)$$

along a straight line  $\mathbf{r}(t) = \mathbf{a}t + \mathbf{b}$  gives rise to a 1D sinusoidal signal (see Figs. 4(a) and 4(b)):

$$s(t) \stackrel{\text{def}}{=} I(\mathbf{r}(t)) = \sum_{k=1}^K \tilde{c}_k e^{j\omega_k t}$$

where  $\tilde{c}_k = c_k e^{j\mathbf{u}_k^T \mathbf{b}}$  and  $\omega_k = \mathbf{u}_k^T \mathbf{a}$ . Note that the frequencies of the 1D samples are the projection of the 2D sinusoidal vectors along the slope of the trajectory.

### B. An Exact Sampling Theorem

Suppose the image is sinusoidal with  $K$  2D sinusoids as defined in (1) and the trajectory is continuous,

$$\mathbf{a}_l t_l + \mathbf{b}_l = \mathbf{a}_{l+1} t_l + \mathbf{b}_{l+1}, \quad l = 1, 2, \dots, L$$

and piecewise-linear consisting of  $L$  stitched straight-line segments

$$\mathbf{r}(t) = \mathbf{a}_l t + \mathbf{b}_l, \quad t \in [t_{l-1}, t_l], \quad l = 1, 2, \dots, L \quad (2)$$

as shown in Fig. 5. In addition, define the 2D image frequency matrix  $\mathbf{U} \in \mathbb{R}^{2 \times K}$ ,  $K \geq 2$ , and trajectory slope matrix  $\mathbf{A} \in \mathbb{R}^{2 \times L}$ ,  $L \geq 2$ , as:  $\mathbf{U} = [\mathbf{u}_1, \mathbf{u}_2 \dots \mathbf{u}_K]$ ,  $\mathbf{A} = [\mathbf{a}_1, \mathbf{a}_2 \dots \mathbf{a}_L]$ . We require that both  $\mathbf{U}$  and  $\mathbf{A}$  are of rank 2; i.e., full-rank.

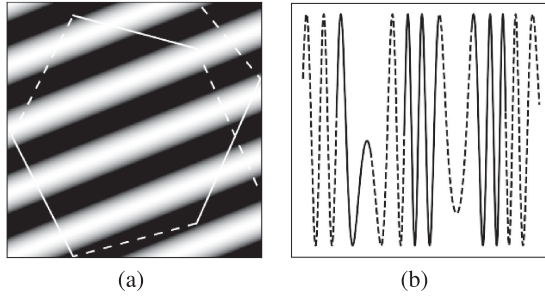


Fig. 5. Exact sampling theorem: (a) Sampling a 2D sinusoidal image ( $K = 1$ ) along a piecewise-linear trajectory; (b) The resulting 1D piecewise sinusoidal signal along a piecewise linear trajectory. Note that we use  $K = 1$  only for visualization purposes ( $K \geq 2$  is necessary in order to retrieve 2D trajectories).

Let  $\omega$  denote the sampling rate and  $T = 2\pi/\omega$  the sampling step. It is straightforward to see that  $\mathbf{r}'(t) = \mathbf{a}_l, t \in [t_{l-1}, t_l]$  represents the velocity of the mobile sensor. Here, we only require uniform speed within line segments, but do not require this speed to be the same between segments. Consequently, the speed can vary arbitrarily between segments. Assume that each segment of the piecewise-linear trajectory is long enough so that

$$S_l \geq 2K \|\mathbf{a}_l\| T, \forall l = 1 \dots L \quad (3)$$

where  $S_l, l \in \{1 \dots L\}$  is the length of the  $l$ -th segment.

$$S_l = \|\mathbf{a}_l\|(t_l - t_{l-1})$$

Since the number  $N_l$  of samples of the  $l$ -th segment of the piecewise-linear trajectory is given by

$$N_l = \frac{S_l}{\|\mathbf{a}_l\| T}, N_l \in \mathbb{Z}$$

(3) ensures that  $N_l$  is larger than  $2K$ . Denoting by  $\omega = 2\pi/T$  the sampling rate, the acquired 1D temporal samples can be expressed as

$$s_{l,n} = \sum_{k=1}^K \tilde{c}_{k,l} e^{j2\pi n \frac{\omega_{k,l}}{\omega}}, \quad n = 0 \dots N_l - 1, l = 1 \dots L \quad (4)$$

where  $\tilde{c}_{k,l} = c_k e^{j\mathbf{u}_k^T \mathbf{b}_l}$  and  $\omega_{k,l} = \mathbf{u}_k^T \mathbf{a}_l$ . Again, the frequencies  $\omega_{k,l}$  of the 1D samples are a projection of the 2D sinusoidal vectors along the velocity. Additionally, we assume that the known sampling rate  $\omega$  is sufficiently large:

$$\omega \geq 2 \max_{l=1,\dots,L} \|\mathbf{a}_l\| \max_{k=1,\dots,K} \|\mathbf{u}_k\|, \quad (5)$$

a condition that is not very restrictive, given that actual sensors can easily achieve sampling rates that are much higher than the equivalent spatial frequencies involved (for mobile sensors moving at speeds of a few m/s).

Under these hypotheses, we have the following sampling theorem:

**Theorem 1** (Exact FRI Sensing): Given uniform 1D temporal samples along an unknown piecewise-linear trajectory, the 2D image and trajectory can be exactly reconstructed up to a 2D affine transformation (shift plus linear distortion).

*Proof:* We present the proof of this theorem by constructing the solution to the problem.

Assume at first that the number of samples per straight-line  $N_l$  and the number of sinusoids  $K$  are known. Then, the portion of 1D temporal signal in each segment is a sum of  $K$  1D sinusoids, as shown in (4). Notice that, the frequencies  $\omega_{k,l}$  of the 1D signal involve the 2D frequencies  $\mathbf{u}_k$  and the slopes of the piecewise-linear trajectory  $\mathbf{a}_l$ .

Given the 1D temporal samples  $s_{l,n}$ , we can exactly retrieve the frequencies  $\{\omega_{k,l}/\omega\}_{k=1\dots K}$  of each segment using Prony's method [23], provided that

$$-\frac{1}{2} \leq \frac{\omega_{k,l}}{\omega} < \frac{1}{2},$$

which results from (5).

Given the frequencies  $\omega_{l,k}$ , we can then retrieve the amplitudes  $\tilde{c}_{l,k}$  by solving the linear system of equations (4).

Then, we order the estimated 1D segment frequencies as a  $K \times L$  matrix  $\Omega$ .

$$\Omega = \begin{bmatrix} \omega_{1,1} & \omega_{1,2} & \cdots & \omega_{1,L} \\ \omega_{2,1} & \omega_{2,2} & \cdots & \omega_{2,L} \\ \vdots & \vdots & \ddots & \vdots \\ \omega_{K,1} & \omega_{K,2} & \cdots & \omega_{K,L} \end{bmatrix} = \underbrace{[\mathbf{u}_1, \mathbf{u}_2 \dots \mathbf{u}_K]^T}_{2 \times K \text{ matrix } \mathbf{U}} \cdot \underbrace{[\mathbf{a}_1, \mathbf{a}_2 \dots \mathbf{a}_L]}_{2 \times L \text{ matrix } \mathbf{A}} \quad (6)$$

Obviously, the matrix  $\Omega$  is at most of rank 2, as the product of two rank-2 matrices. Moreover, it cannot be of lower rank because, otherwise,  $\mathbf{A} = (\mathbf{U}\mathbf{U}^T)^{-1}\mathbf{U}\Omega$  would not be rank-2 (note that, by hypothesis, both  $\mathbf{A}$  and  $\mathbf{U}$  are rank-2).

This rank property captures precisely the nature of the redundancy that exists in the stream of estimated 1D frequencies, and suggests a simple way, through matrix factorization, to retrieve the trajectory slopes and image frequencies. Using, e.g., singular value decomposition, it is possible to express  $\Omega$  as  $\mathbf{U}_0^T \mathbf{A}_0$  where  $\mathbf{A}_0$  and the unitary<sup>2</sup> matrix  $\mathbf{U}_0$  are of dimension  $2 \times L$  and  $2 \times K$ , respectively. This factorization is not unique, however it can easily be shown that all its possible solutions are given by

$$\mathbf{U}' = \mathbf{Q}^{-T} \mathbf{U}_0, \quad \mathbf{A}' = \mathbf{Q} \mathbf{A}_0$$

where  $\mathbf{Q}$  is an arbitrary invertible matrix. To see this, it suffices to equate the factorization  $\mathbf{U}'^T \mathbf{A}'$  with  $\mathbf{U}_0^T \mathbf{A}_0$ . Multiplying left by  $\mathbf{U}_0$  leads to  $\mathbf{A}_0 = \mathbf{U}_0 \mathbf{U}'^T \mathbf{A}'$ , where the  $2 \times 2$  matrix  $\mathbf{U}_0 \mathbf{U}'^T$  is invertible (since  $\mathbf{A}_0$  is rank-2). Denoting by  $\mathbf{Q}$  its inverse, we find  $\mathbf{A}' = \mathbf{Q} \mathbf{A}_0$ , and then  $\mathbf{U}' = \mathbf{Q}^{-T} \mathbf{U}_0$ .

We have shown that, once the 1D frequencies identified in each segment are correctly paired between segments, the piecewise-linear trajectory solution to our problem is unique, up to an affine transformation. What if different pairings were valid? This is indeed possible, but we claim that this “almost” never happens, when considering all sets of  $\{\mathbf{u}_k, \mathbf{a}_k\}_{k=1\dots K}$ . More specifically, consider an arbitrary rank-2 matrix with

<sup>2</sup>i.e.,  $\mathbf{U}_0 \mathbf{U}_0^T = \mathbf{Id}$ .

columns  $[\omega_1, \omega_2, \dots, \omega_L]$ , where  $\omega_j = [\omega_{i,j}]_{1 \leq i \leq K}$ , and denote by  $\pi_j^\omega = [\omega_{\pi_j(i),j}]_{1 \leq i \leq K}$  the vector  $\omega_j$  with  $\pi_j$ -permuted coordinates. We claim that, unless the permutations (“pairings”)  $\pi_j$  are all identity, the matrix  $[\pi_1^\omega, \pi_2^\omega, \dots, \pi_{L-1}^\omega, \omega_L]$  is “almost” always of rank  $\geq 3$ . Sketch of a proof:

- 1) it is sufficient to consider the case of three vectors only;
- 2) all possible rank-2 matrices are of the form  $[\omega_1, \omega_2, a_1\omega_1 + a_2\omega_2]$ , where  $(\omega_1, \omega_2, a_1, a_2) \in \mathbb{R}^{2K+2}$ ;
- 3) for any two permutations  $\pi_1$  and  $\pi_2$  that are not both identity, the set of elements of  $\mathbb{R}^{2K+2}$  for which  $[\omega_1, \pi_1^\omega, \omega_2, \pi_2^\omega]$  is of rank-2 has zero Lebesgue measure;
- 4) as a consequence, the set of coefficients  $a_1, a_2$  for which  $a_1\omega_1 + a_2\omega_2 = a'_1\pi_1^\omega + a'_2\pi_2^\omega$  is “almost” always of dimension equal to one or zero; this dimension is strictly smaller than the dimension two of  $\text{span}\{\omega_1, \omega_2\}$ , which shows that  $[\pi_1^\omega, \pi_2^\omega, a_1\omega_1 + a_2\omega_2]$  is “almost” always of rank-3;
- 5) cycling over the finite number of all (non-both identity) permutations shows that, even if  $[\omega_1, \omega_2, \omega_3]$  is of rank-2,  $[\pi_1^\omega, \pi_2^\omega, \omega_3]$  is “almost” never of rank-2.

Hence, we can retrieve the 2D frequencies,  $\{\mathbf{u}_k\}_{k=1\dots K}$ , of the image and the direction vectors,  $\{\mathbf{a}_l\}_{l=1\dots L}$ , of the trajectory, up to a linear transformation  $\mathbf{Q}$ . Since the trajectory is continuous, the parameters  $\mathbf{b}_l$  in (2) can be retrieved up to a unique shift; i.e., the trajectory can be retrieved up to an affine transformation. Eventually, the coefficients  $c_k$  of the individual 2D frequency components result from  $c_k = \tilde{c}_{k,l} e^{-j\mathbf{u}_k^T \mathbf{b}_l}$ , which allows to reconstruct the image.

Now, how to determine the number  $K$  of sinusoids, the signal segmentation  $\{N_l\}_{l=1\dots L}$  and the pairing of frequencies  $\{\omega_{k,l}\}_{l=1\dots L}$ ? Our solution builds upon the property that  $2K+1$  uniform samples of a sum of  $K$  exponentials can be used to build a  $(K+1) \times (K+1)$  Toeplitz matrix whose rank is exactly  $K$  [23]:

- For each  $K$ , we can scan all consecutive groups of  $2K+1$  samples and check whether some of them build a rank- $K$  matrix: the smallest value of  $K$  for which this happens is going to be our solution.
- When a group of  $2K+1$  consecutive samples does not result in a rank- $K$  matrix, we know that this is because these samples belong to two distinct line segments: this allows to determine both the number of segments, and their start/end samples.
- Pairing correctly the 1D frequencies  $\{\omega_{k,l}\}_{l=1\dots L}$  can be achieved by trying all possible orderings of the columns of the matrix  $\Omega$  in (6) and retaining only the one for which  $\Omega$  is of rank 2.

A global view of the entire solution is shown in Fig. 6. ■

As shown before, the trajectory reconstruction problem can be solved only up to an affine transformation (6 parameters). One possible way to eliminate this indeterminacy is to use extra information that would allow to retrieve these 6 parameters. For example, the ground-truth positions of three points (e.g., the

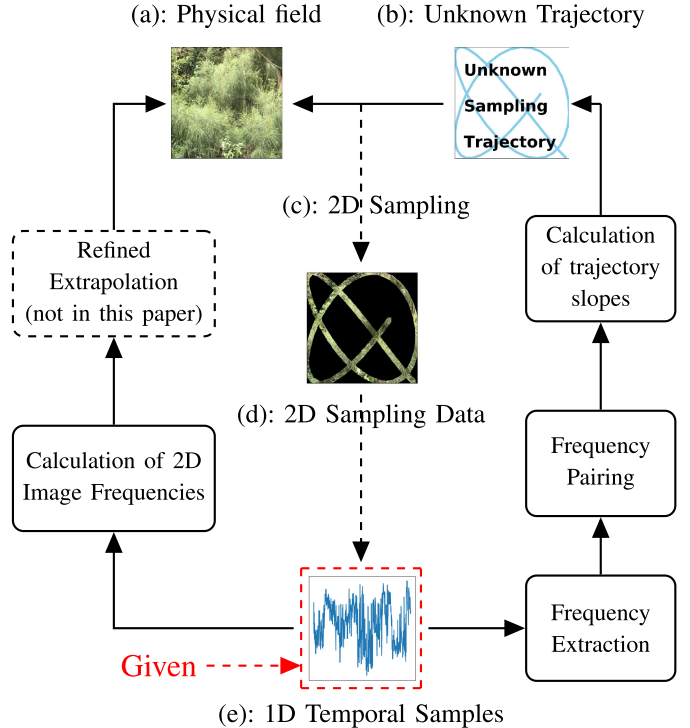


Fig. 6. Flowchart of the solution construction in the FRI Sensing theorem: the 2D sinusoidal image and piecewise linear trajectory can be exactly reconstructed (up to an affine transformation).

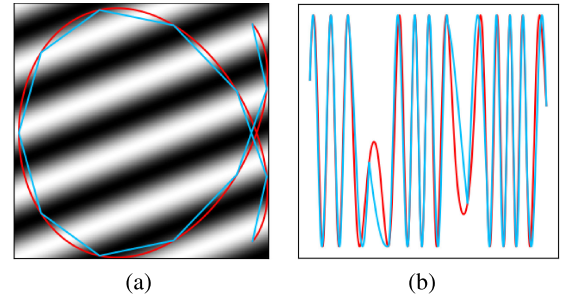


Fig. 7. Linear approximation of non-straight line sampling: (a) Piecewise linear approximation (blue) of the curved trajectory (red). (b) The resulting approximate 1D time series (red: ground truth, blue: approximate).

starting and end points, and an intermediate one) of the trajectory would be sufficient.

### C. Generalization to Real Trajectories

Our exact sampling theorem only applies to piecewise-linear trajectories, while the actual situation is richer and more diverse. Hence, we need to limit the diversity by imposing hypotheses on the trajectory and the 2D physical field represented as an image.

We will see that under specific hypotheses, it is still possible to apply the exact sampling framework and achieve trajectory reconstruction with a reasonable accuracy. A typical assumption is that the trajectory is twice differentiable but sufficiently straight locally (see Fig. 7) so that we can approximate it as a

piecewise-linear trajectory, so as to be able to apply Thm. 1 and the associated algorithm.

Obviously, the hypotheses on the trajectory and the image should be closely interrelated: for example, if the trajectory is more rugged, then the image should change faster in space (because the line segments should be shorter). Developing this observation, we list the following main ingredients that are likely to influence the reconstruction accuracy:

1) Trajectory-related:

- a) Acceleration of the mobile sensor:  $\max_t \|\mathbf{r}''(t)\| \leq \gamma_0$ .

At fixed sensor speed ( $\|\mathbf{r}'(t)\| = \text{constant}$ ), the larger the acceleration, the smaller the radius of curvature of the trajectory as a result of the equality  $\kappa(t) = \|\mathbf{r}''(t)\|/\|\mathbf{r}'(t)\|^2$  (see Appendix A). As a result, the image should change faster due to shortened trajectory segments.

- b) Velocity of the mobile sensor:  $\min_t \|\mathbf{r}'(t)\| \geq v_0$ .

At fixed sampling rate, the slower the mobile sensor, the smaller the trajectory segment. Then, the 2D image sinusoids should change faster within shorter trajectory segments, in order for their frequencies to be sufficiently different.

2) Image-related

- a) Spatial variations of the image

At fixed trajectory, faster image variations allow shorter line segments, hence closer curve approximation.

- b) Spatial frequency contents

If the 2D image sinusoids are close to each other, then they behave essentially like only one sinusoid which is insufficient to retrieve the trajectory geometries (we require  $K \geq 2$ ). Besides, the 2D sinusoids to retrieve should have large amplitude to guarantee the estimation robustness and accuracy. To quantify this concept, we define the “conditioning” of the image as

$$\text{cond}\{I\} \stackrel{\text{def}}{=} \min_{k_1, k_2} \frac{1}{\lambda_{k_1, k_2}} \sqrt{\frac{1}{|c_{k_1}|^2} + \frac{1}{|c_{k_2}|^2}}, \quad (7)$$

where  $\lambda_{k_1, k_2}$  is the smallest singular value of the square matrix  $[\mathbf{u}_{k_1}, \mathbf{u}_{k_2}], k_1, k_2 \in \{1 \dots K\}$  (see Appendix B for a justification).

3) Mobile sensor-related

- a) Measurement accuracy  $\sigma_{\text{noise}}$ .

The noise level that corrupts the samples of the mobile sensor, which should be easily obtained from the sensor hardware configuration.

- b) Sampling step  $T$ .

If the sampling step is too large, we may not have enough samples within a trajectory segment. As a result, we may have to increase the length of every trajectory segment and, as a consequence, the reconstruction error will increase.

Now, it is necessary to quantify the interplay between all these ingredients, and how much each of them influences the

final measure that we are interested in: the approximation error between our trajectory estimate and the ground-truth trajectory. Here, for simplification purposes, we are going to deal with the trajectory estimation as if the errors were caused by random fluctuations, despite the fact that the most significant contribution to the error is caused by the inaccuracy of the piecewise-linear approximation (which is deterministic). This is the reason why, the following theorem is stated as a statistical result.

*Theorem 2 (Aproximate FRI Sensing):* Given a sequence of uniform 1D time samples (sampling step  $T$ ) of a 2D sinusoidal image (1) along an unknown curved trajectory  $\mathbf{r}(t)$ , a piecewise linear approximation of the trajectory ( $L$  segments, with  $N$  samples per segment) can be reconstructed up to an affine transformation with an error of standard deviation

$$\begin{aligned} \text{std}\{\mathbf{r}(t)\} &\leq \frac{2\sqrt{3}L\sigma}{\sqrt{N}} \text{cond}\{I\} + \frac{\gamma_0 N^2 T^2}{8}, \\ \sigma &\stackrel{\text{def}}{=} \sqrt{\mathcal{E}\{|I|^2\} \|\mathbf{U}\|_F^2 N^4 T^4 \gamma_0^2 / 64 + \sigma_{\text{noise}}^2} \end{aligned} \quad (8)$$

Here  $\mathcal{E}\{|I|^2\} = \sum_k |c_k|^2$  is the average power of the image  $I(\mathbf{r})$ ,  $\sigma_{\text{noise}}^2$  is the variance of the measurement noise,  $\|\mathbf{U}\|_F^2 = \sum_{k=1}^K \|\mathbf{u}_k\|^2$ ,  $\text{cond}\{I\}$  is defined by (7), and  $\gamma_0$  is an upper bound on the second order derivative of  $\mathbf{r}(t)$ .

The proof (see Appendix B) relies on the use of an efficient frequency estimation algorithm (able to reach Cramér-Rao lower bounds [24]) in the algorithmic framework of Fig. 6.

One of the hidden conditions for this result to hold is that the 1D frequencies identified in each segment are sufficiently distinct, a condition which is favored by ensuring that  $v_0 = \min_t \|\mathbf{r}'(t)\|$  is not too small.

Obviously, in a practical setting, this standard deviation becomes a quantitative predictor of the error between the ground-truth curve and the piecewise-linear approximation found by our algorithm. There is a difference, however, between the hypotheses involved in Thm. 2, which assume the knowledge of the spatial frequencies  $\mathbf{u}_k$  of the image, and the conditions of the algorithm that we are developing in this article, which do not: as we have pointed out, finding both the trajectory and the parameters of the image can be done only up to an affine transformation, which is the reason why we define a specific affine-invariant approximation error (10) in the validation part of this article (Section IV)—different from the standard deviation above. Yet, as we will see in Section IV, (8) is a reasonably fair predictor of the accuracy of our algorithm.

A few observations: first, the smaller the sampling step  $T$ , the more accurate the final trajectory reconstruction; second, keeping the same image power, the “better conditioned” the image is (i.e., the more “different” its frequencies are), the more accurate the reconstruction; next, we can clearly see that a smaller acceleration gives rise to a lower reconstruction uncertainty, which is consistent with the previous analysis; last, possible outliers in the estimated 1D frequencies (frequent in natural images) may be ruled out based on the frequency continuity implied by our bounded acceleration assumption.

### III. ALGORITHMIC SETTING

Throughout the process, frequency estimation and frequency pairing are the two most important parts which highly influence the final reconstruction quality and take up most of the runtime. Therefore, accurate, robust and fast algorithms for estimating and pairing frequencies are essential to the accurate reconstruction of the 2D trajectory and the 2D sinusoidal image. Here, we refer to frequency estimation as FRI approximation [23] because of the relation between this problem and that of estimating the “innovations” (i.e., sparse activation times) of 1D signals.

#### A. FRI Approximation

Approximating a 1D signal as a sum of  $K$  sinusoids is what enables the entire FRI sensing framework. It directly determines the performance of the reconstruction algorithm and requires high precision and strong robustness.

High-resolution frequency estimation is a classical signal processing problem that has been thoroughly studied in the 1970–1990s [25], [26], [27], [28]. The algorithms developed to that purpose can, in principle, be used in our context. However, even if they are sufficiently accurate to retrieve frequencies of sinusoids in noise, they are not robust enough to approximate non-sinusoidal signals as a sum of sinusoids. Fortunately, we have recently developed a very accurate, fast and robust algorithm for doing just that [29], [30].

1) *Estimation of Sinusoids:* We introduce our frequency estimation algorithm which is based on model fitting [29]. The key idea is to consider that any  $K$ -sinusoidal approximation that is close enough (within a “noise” margin) to the measured samples is a valid solution to our problem. More specifically, we consider the FRI recovery to be successful as soon as the criterion

$$\text{MSE}_{\text{rec}} \leq \sigma_{\text{noise}}^2 \quad (9)$$

is satisfied, where  $\text{MSE}_{\text{rec}}$  is the mean square error (MSE) between the reconstructed samples and the 1D mobile sensor samples,  $s_{l,n}$ . In consistence with Section II-C,  $\sigma_{\text{noise}}^2$  denotes the input MSE that represents the “noise” (or, more generally, “mismatch”) level.

The second idea is that the DFT of a sum of  $K$  sinusoids can be expressed as fraction of two polynomials in  $e^{-j2\pi n/N}$  ( $N$  = number of samples,  $n$  = frequency index): a numerator polynomial  $P_{K-1}$  of degree  $K-1$  and a denominator  $Q_K$  of degree  $K$ . Due to the unitarity of the DFT (Parseval’s identity), we can use this ratio structure as a model and perform model-fitting on the DFT of the signal samples.

$$\min_{Q_{K-1}, P_K} \sum_{n=0}^{N-1} \left| \hat{s}_{l,n} - \frac{P_{K-1}(e^{-j2\pi n/N})}{Q_K(e^{-j2\pi n/N})} \right|^2$$

where  $\hat{s}_{l,n}$  denotes the Discrete Fourier Transform of the signal  $s_{l,n}$ . In fact, the polynomial  $Q_K$  is the annihilation filter in [23] whose zeros uniquely define the frequencies  $\omega_{k,l}$  of the 1D signal.

Solving the following quadratic minimization problem for  $Q_K^i$

$$\min_{Q_K^i, P_{K-1}^i} \sum_{n=0}^{N-1} \left| \frac{Q_K^i(e^{-j2\pi n/N}) \hat{s}_{l,n} - P_{K-1}^i(e^{-j2\pi n/N})}{Q_K^{(i-1)}(e^{-j2\pi n/N})} \right|^2$$

provides a collection of candidates for  $Q_K$ , when  $i = 1 \dots i_{\max}$ , out of which we choose the one for which the MSE is the smallest. Changing initialization of these iterations provides even more candidates. Typically, two random initializations and  $i_{\max} = 20$  are sufficient to obtain a solution that is within the expected noise margin. Please refer to [29], [31] for more details.

2) *Model Order:* Our postulate is that any sum of  $K$  sinusoids that fits our samples within a given noise margin is a valid solution. Hence, applying a parsimony principle, it is possible to determine that the “best” model order is the smallest value of  $K$  for which this sum of sinusoids is a valid solution. An efficient implementation of this principle uses a dichotomous approach that is described in [31].

3) *Consistency of the Frequency Estimation Results:* Plots (see Fig. 8) of the 1D frequencies estimated from the 1D samples of an image along the trajectory of a mobile sensor show the intrinsic consistency of the 2D frequencies  $\mathbf{u}_k$  of the physical field.

As expected, when the image is a sum of pure 2D sinusoids, the associated 1D frequencies are “consistent” across all the segments of the trajectory, as can be seen in Fig. 8 (a): visually, each individual frequency can be followed by continuity across trajectory segments. But even if the image is not so simple, there is still some consistency between consecutive segments: see Figs. 8 (b) and (c). This correlation detected by our algorithm provides the possibility for the final 2D trajectory and image reconstruction, when enough distinct frequencies can be paired between segments (i.e., in Fig. 8 (b), but not in Fig. 8 (c)).

#### B. Frequency Pairing

1) *Amplitude Criterion:* Although we did not mention it earlier, pairing the frequencies found in different segments is not straightforward. There are several clues that could help identify which frequency  $\{\omega_{k,l}\}_{k=1\dots K}$  in segment  $l$  corresponds to which frequency  $\{\omega_{k,l'}\}_{k=1\dots K}$  in segment  $l'$ . One available clue is that, since the amplitude  $\tilde{c}_{k,l}$  of the sinusoid  $\omega_{k,l}$  is attached to the frequency  $\mathbf{u}_k$ , its modulus should be invariant across segments. This provides a simple criterion for frequency pairing: find all the frequencies across segments with the same amplitude modulus.

However, due to the approximation error, the amplitude estimation is not robust enough under noise effects and hence, cannot be used alone for pairing purposes. This is an intrinsic limitation that can be predicted by computing the Cramér-Rao bounds of the parametric estimation problem: the uncertainty over the amplitudes is significantly larger than the uncertainty over the frequencies [23].

2) *Rank Criterion:* Another clue is that, when the 1D frequencies have been paired accurately, the frequency matrix  $\Omega$  should be of rank-2—or in the situation of inaccuracies, can be approximated accurately by a rank-2 matrix. This provides

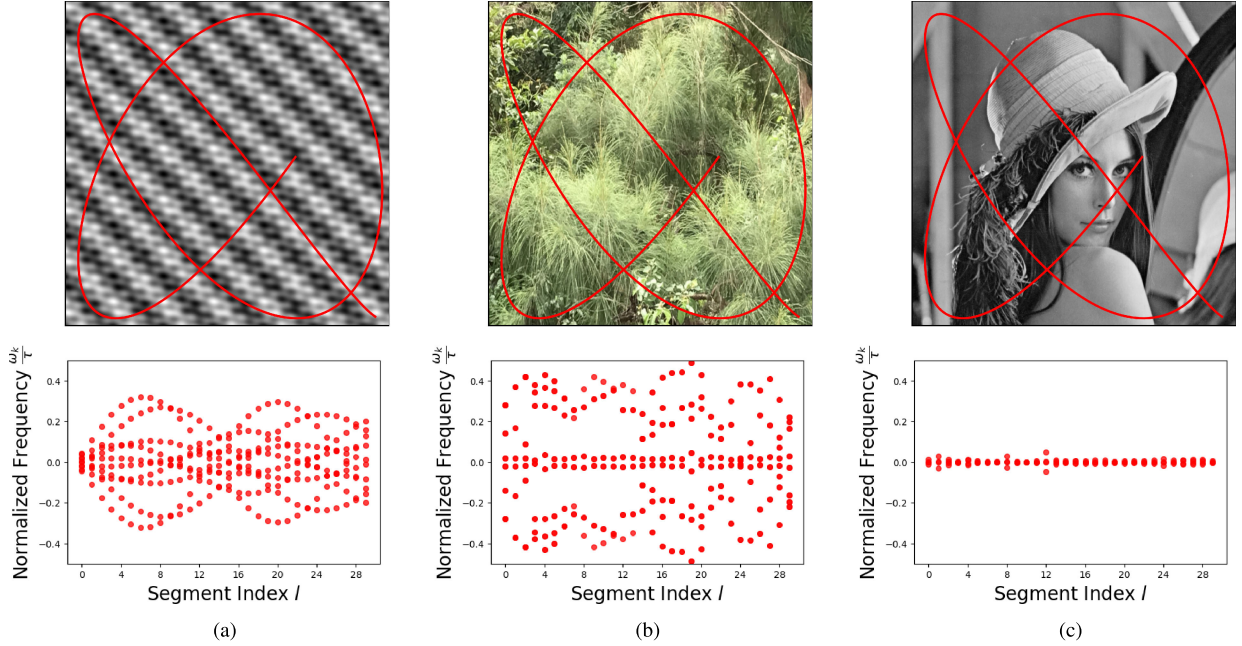


Fig. 8. Estimated 1D frequencies (bottom plot, normalized to  $[-0.5, 0.5]$ ) from an image made of (top): (a) a sum of ten 2D sinusoids; (b) high-frequency natural textures; and (c) low-frequency natural textures. In these figures, we can follow some of the frequencies individually by visual continuity across segments.

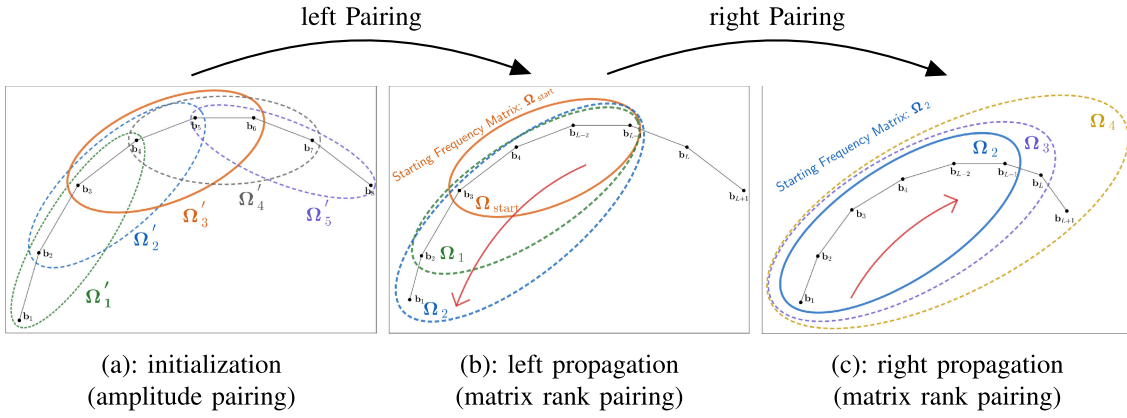


Fig. 9. FRI Sensing Pairing Algorithm: (a) the matrices  $\Omega'_l$  are built with the frequencies ordered according to their amplitude; then, the group of 3 consecutive segments for which  $\Omega'_l$  is closest to rank 2  $\rightsquigarrow \Omega_{\text{start}}$ . (b) Starting from the initial frequency matrix  $\Omega_{\text{start}}$ , the frequencies found in each new leftward segment,  $l$ , are appended to  $\Omega_{l-1}$  and ordered so as to minimize the rank of  $\Omega_l$ . (c) Similar extension of the frequency matrix  $\Omega_l$  by processing segments to the right.

another criterion for frequency pairing: find the pairing that maximises the ratio between the second and third largest singular value of the matrix  $\Omega$ .

In order to reduce the computational cost of this strategy, we choose to pair only a smaller subset  $K_0$  of the  $K$  sinusoids that have the largest absolute amplitudes. A value of  $K_0 = 5$  is a good compromise between accuracy (larger  $K_0$  increases accuracy) and computational cost.

Fig. 9 intuitively describes the process of the proposed pairing algorithm. Notice that, after the initialization, the processing order does not matter. In other words, whether starting with the left (or right) propagation or alternate left and right processing will not affect the final paired results. Here, for convenience we first process segments to the left and then extend to the right propagation after the initialization of  $\Omega_{\text{start}}$ .

### C. Reconstruction of the Trajectory

After the construction of  $\Omega$  based on the pairing algorithm, we can obtain the estimated trajectory slopes by approximating  $\Omega$  with a rank-2 matrix using the SVD algorithm, and keeping only the two largest singular values and the related vectors. This rank-2 approximation is equivalent to the factorization (6) which provides two matrices,  $\mathbf{U}$  and  $\mathbf{A}$ , where the  $2 \times L$  matrix  $\mathbf{A}$  contains the information on the slopes of the piecewise segments that approximate the curved trajectory.

With the retrieved curve slopes, the sampling trajectory can be reconstructed as:

$$\mathbf{r}(t) = \mathbf{a}_l t + \mathbf{b}_l, \quad t \in [t_{l-1}, t_l], \quad l = 1 \dots L,$$

where  $\mathbf{b}_1$  is arbitrary and the other vectors  $\mathbf{b}_l$  are obtained by induction:  $\mathbf{b}_{l+1} = NT\mathbf{a}_l + \mathbf{b}_l$ .

**Algorithm 1:** Pairing Algorithm for FRI Sensing.

---

1D sinusoids  $\{\omega_{k,l}\}_{k=1\dots K}^{l=1\dots L}$ , paired sinusoid number  $K_0$

- 1: **for**  $l = 1$  to number of segments **do**
- 2:   Select  $K_0$  the 1D sinusoids with the largest amplitude  $\sim \{\omega_{k,l}\}_{k=1\dots K_0}$
- 3: **end for**
- Initialization** Select and pair 3 consecutive segments based on the amplitude pairing as the initial frequency matrix  $\Omega_{\text{start}}$ , denote the corresponding segment index as  $l_{\text{start}}$ .
- 4: Left Pairing Propagation
- 5: **for**  $l = 1$  to  $l_{\text{start}} - 1$  **do**
- 6:   Pair the  $l$ -th segment frequencies based on the rank criterion.
- 7:   Attach the paired segment frequencies as a new column to the frequency matrix:  
 $\Omega_l \leftarrow [\{\omega_{k,l}\}_{k=1\dots K_0}, \Omega_{l-1}]$
- 8: **end for**
- 9: Right Pairing Propagation
- 10: **for**  $l = l_{\text{start}}$  to number of segments **do**
- 11:   Pair the  $l$ -th segment frequencies based on the rank criterion.
- 12:   Attach the paired segment frequencies as a new column to the frequency matrix:  
 $\Omega_l \leftarrow [\Omega_{l-1}, \{\omega_{k,l}\}_{k=1\dots K_0}]$ .
- 13: **end for**

**Output:** The paired frequency matrix  $\Omega$ .

---

Together with the estimated trajectory slopes, we can obtain the estimated 2D image sinusoids  $\mathbf{U}$  at the same time. Through least squares, the amplitudes associated to the frequencies can be found accurately and efficiently. Combining them together, the 2D sinusoidal physical field can be recovered effectively according to equation (1).

#### IV. ALGORITHM VALIDATION

In this section, we demonstrate that the proposed algorithm is effectively able to retrieve the 2D geometry of the trajectory of a mobile sensor from the mere sequence of samples of the image/field along that trajectory, and under various conditions. To perform these tests, we have implemented our algorithm in python on a MacBook Pro 2015 with a 4-core CPU and 16 GB of RAM. In all the cases, we have used the 2D sinusoidal image made of 10 different frequencies sampled on a  $330 \times 280$  grid as shown in Fig. 8(a).

##### A. Evaluation Metrics

In order to characterise the accuracy of our algorithm, we need to quantify the error between the reconstructed trajectory  $\mathbf{r}(t)$  and the ground-truth trajectory  $\mathbf{r}_0(t)$ . Given the affine invariance of our problem, we should in principle use a distance of the form

$$\min_{\mathbf{Q} \in \mathbb{R}^{2 \times 2}, \mathbf{q} \in \mathbb{R}^2} \frac{\left( \int \inf_{t'} \|\mathbf{r}_0(t) - \mathbf{Q}\mathbf{r}(t') - \mathbf{q}\|^2 dt' \right)^{1/2}}{\|\mathbf{r}_0(t)\|_2}$$

but for the sake of simplicity, we choose the same parameter for the two trajectories. Hence, we define the curve reconstruction error as follows:

$$\text{err}\{\mathbf{r}, \mathbf{r}_0\} = \min_{\mathbf{Q} \in \mathbb{R}^{2 \times 2}, \mathbf{q} \in \mathbb{R}^2} \frac{\|\mathbf{r}_0(t) - \mathbf{Q}\mathbf{r}(t) - \mathbf{q}\|_2}{\|\mathbf{r}_0(t)\|_2}. \quad (10)$$

##### B. FRI Sensing

1) *FRI Sensing With Noiseless Image*: As expected, when the image is a sum of 2D sinusoids and the trajectory is piecewise linear, the proposed algorithm can achieve a reconstruction close to machine precision ( $\text{err}\{\mathbf{r}, \mathbf{r}_0\} \approx 10^{-12}$ ), with a computation time of approximately 0.2 seconds. Visually we cannot tell the difference between the reconstruction and the ground truth. This experiment validates the exact sampling theorem and the accurate implementation of our algorithm.

##### C. Sampling Theorem Validation

Then, we validate Thm. 2 by conducting the following simulations:

- 1) Dependence of the reconstruction error on the radius of curvature of the trajectory.
- 2) Dependence of the reconstruction error on the variance  $\sigma_{\text{noise}}^2$  of the noise.
- 3) Dependence of the reconstruction error on the length of the trajectory.

In each experiment, we only manipulate one variable while keeping the others unchanged.

1) *Effect of the Curvature Radius*: In this experiment, the sampling trajectory is parametrised according to:

$$\mathbf{r}_0(t) = \frac{1}{\kappa} \begin{bmatrix} \cos(t) - \cos(\beta t) \\ \sin(t) - \sin(\beta t) \end{bmatrix}$$

where  $\beta \ll 1$  is a small number, so that the actual curvature of this parametric curve is close to the value of  $\kappa$  that we choose. Fig. 10 shows how the trajectory reconstruction error changes with the curvature. We have averaged the approximation error obtained over 10 different shifts of the trajectory, so as to have a value that is more representative of the intrinsic error expected with our algorithm. As can be seen, in all cases the trajectory is recovered quite accurately. In addition, the 2D sinusoidal image can also be reconstructed, and the resulting PSNR varies from 17.02 dB (smallest curvature radius) to 32.58 dB (larger curvature radius).

Obviously, as the curvature of the trajectory gets smaller, the final reconstruction gets more accurate. Notice that, when  $\kappa \leq 1/2$ , the obtained reconstruction error  $\text{err}\{\mathbf{r}, \mathbf{r}_0\}$  is parallel and reasonably close to the upper bound (8), after normalization by  $\|\mathbf{r}_0\|$ .

Notice that, the reconstruction error increases sharply when  $\kappa > 1/2$ ; i.e., when the wavelengths of the 2D image sinusoids are comparable to the individual trajectory segment length, resulting in insufficient image variation within each trajectory segment. This effect is cumulated with the increase of the piecewise-linear model inaccuracy that results from a smaller curvature radius.

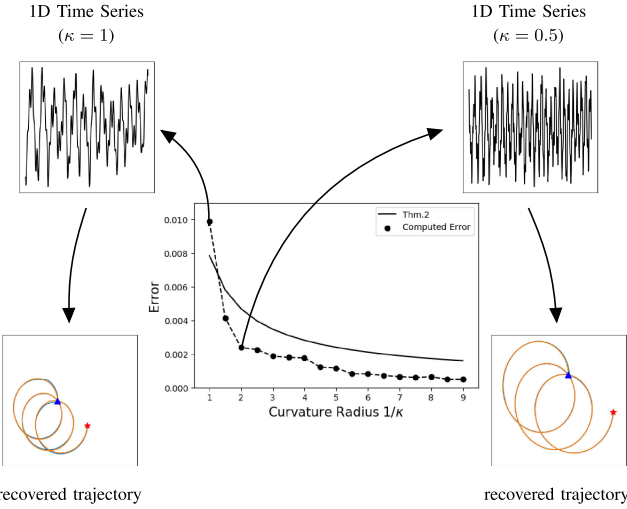


Fig. 10. Center: reconstruction error  $\text{err}\{\mathbf{r}, \mathbf{r}_0\}$  vs curvature radius  $1/\kappa$  of the trajectory. Top: sensor time samples. Bottom: ground truth trajectory shown in red, reconstructed trajectory shown in blue (start point: blue triangle, end point: red star). Each data point is the average of 10 independent tests with random spatial shifts.  $\beta = 1/\pi^2$ .

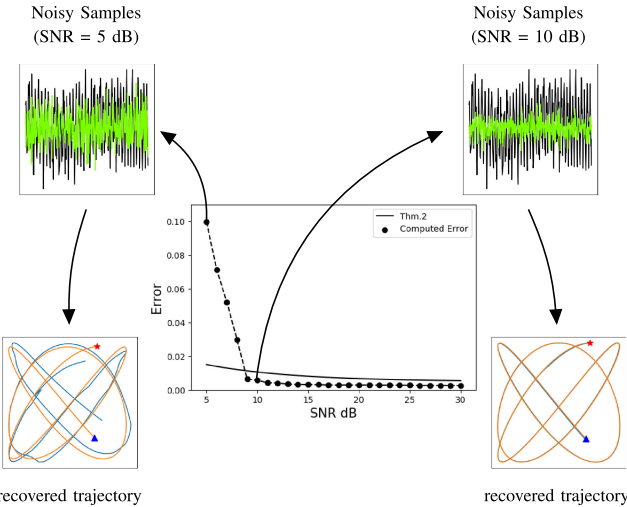


Fig. 11. Center: reconstruction error  $\text{err}\{\mathbf{r}, \mathbf{r}_0\}$  vs noise level. Top: Noisy sensor time samples (black) overlayed with the noise signal (green). Bottom: ground truth trajectory shown in red, reconstructed trajectory shown in blue (start point: blue triangle, end point: red star). Each data point is the average of 10 independent tests with random spatial shifts.  $\beta = \sqrt{\pi}/5$ .

**2) Effect of Noise:** In this part, we add noise to the sampled 1D time series at different levels (SNR from 5 dB to 30 dB). Fig. 11 reveals how the trajectory reconstruction error changes over different noise levels. Again, the image can also be reconstructed with PSNR values ranging from 10.87 dB to 27.13 dB depending on the noise level.

Notice that, although the resulting 1D time series is quite noisy (SNR: 5 dB), the proposed algorithm can still reveal the geometric shape of the trajectory. This shows that the proposed algorithm is robust and accurate against noise interference. Moreover, after a certain threshold (around 9 dB), even though the resulting 1D time series is still quite noisy, the reconstruction error falls below the error bound calculated in Thm. 2. The

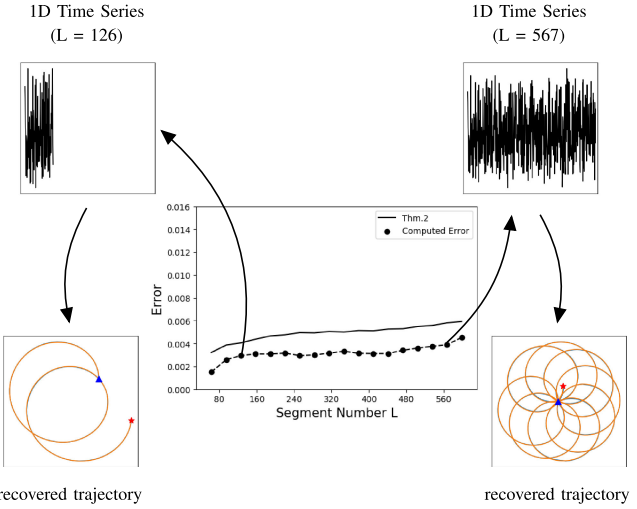


Fig. 12. Center: reconstruction error  $\text{err}\{\mathbf{r}, \mathbf{r}_0\}$  vs length of the trajectory (total number of segments  $L$ ). Top: sensor time samples. Bottom: ground truth trajectory shown in red, reconstructed trajectory shown in blue (start point: blue triangle, end point: red star). Each data point is the average of 10 independent tests with random spatial shifts.  $\beta = 1/\pi^2$ .

“phase transition” between 5 and 9 dB essentially results from the increasing number of frequency pairing mismatch cases between consecutive segments.

**3) Effect of the Length of the Trajectory:** Error accumulation is expected in our algorithm since what is estimated is essentially the derivative  $\mathbf{r}'(t)$  of the trajectory, and Thm. 2 predicts this drift to be affine with respect to the number  $L$  of segments.

Fig. 12 shows that the shape of the calculated upper bound is parallel to the experimental error. The image can be reconstructed with PSNR value varying from 19.79 dB to 20.29 dB. Notice that the error accumulation rate is really small as the error only increases by half while the length of the trajectory increases 7 times. The reconstruction error is so small that it is not possible to distinguish between the ground truth (red) and the reconstructed (blue) trajectories.

## V. DISCUSSION

Interestingly, although we developed the theory for sums of 2D sinusoids, we observe that our algorithm is working accurately for real textured images as well (see Fig. 13). Obviously, the low-order sinusoidal model that justifies our theory does not apply here. Yet, it would not be adequate to consider the natural image model as a high-order sinusoidal representation, since the same could be claimed of many other dense models like spline/wavelet/RBF representations or simply, cosine representations. More likely, natural images exhibit some (slowly changing) local scale and directional footprints that can still be accurately captured by our FRI algorithm, although the exact properties at stake here are still elusive. The test image (bamboo trees,  $3159 \times 2504$  pixels) shown in Fig. 13(a) is taken by us with the camera of an iPhone-7, and the whole computation time is about 24 seconds.

Our finding is that when the resolution of the natural texture images is large enough (empirically  $\geq 10^6$  pixels), the proposed

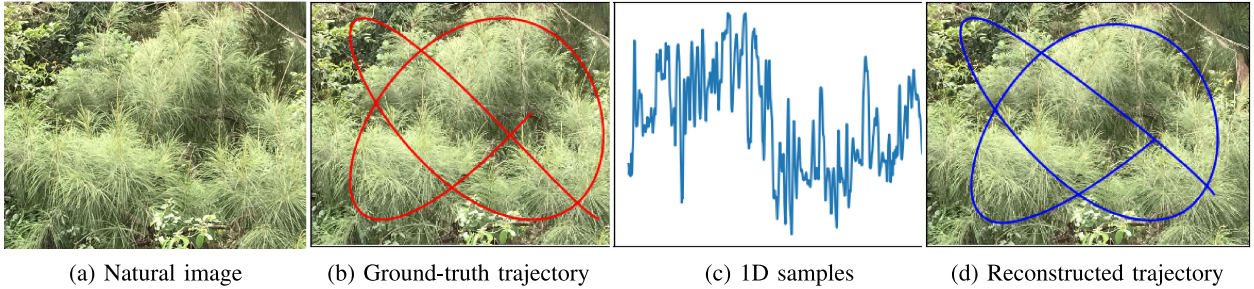


Fig. 13. Recovering a trajectory from the 1D samples of a natural image. (a) Bamboo tree image ( $3159 \times 2504$  pixels). (b) Ground truth sampling trajectory. (c) Image samples along the trajectory in (b). (d) Reconstructed trajectory (error  $\text{err}\{\mathbf{r}, \mathbf{r}_0\} = 0.059$ ).

method can work to some extent. For lower resolution images (e.g.,  $512 \times 512$  pixels), the algorithm is less accurate because there are not enough samples along local trajectory segments. However, what we aim at is physical sampling of a real 2D physical field by a real mobile sensor which usually has such a fine sampling density: this is actually what we simulated in Section IV and we could then use images of size  $330 \times 280$ . Therefore, the sample number limitation is likely an artificial issue in practical sensor applications.

When the image is 2D sinusoidal, the physical field/image can be accurately reconstructed although we did not emphasize this aspect so much in this article. Yet, despite a relatively accurate trajectory reconstruction, natural images cannot yet be accurately reconstructed, a problem on which we are actively working, but is beyond the scope of this article.

## VI. CONCLUSION

In this article we have shown that it is possible to unveil the multidimensional information hidden within a 1D signal obtained by sampling a 2D field/image along some trajectory. Solving this problem would not be possible without strong sparsity hypotheses (typically, on the frequencies of the image and the representation of the trajectory) for which we have developed earlier a very accurate and efficient ‘‘Finite Rate of Innovation’’ (FRI) algorithm—hence, our ‘‘FRI sensing’’ terminology. We have shown how to combine this algorithm with a very accurate frequency pairing strategy so as to solve exactly the FRI sensing problem when the trajectory is piecewise-linear. We have also shown that this limited setting can be generalized to other trajectories and demonstrated the accuracy and robustness of our algorithm in various experiments. Even more interesting, we observed that this algorithm is still accurate on images that are not sums of sinusoids.

## APPENDIX A

### LINK BETWEEN CURVATURE, ACCELERATION, AND VELOCITY

Let  $\kappa$  denote the curvature (i.e., the inverse of the radius of curvature) of the trajectory:

$$\kappa(t) = \frac{|x'(t)y''(t) - x''(t)y'(t)|}{(x'(t)^2 + y'(t)^2)^{\frac{3}{2}}} \quad (11)$$

Using the identity

$$\underbrace{(x'(t)^2 + y'(t)^2)}_{\|\mathbf{r}'(t)\|^2} \underbrace{(x''(t)^2 + y''(t)^2)}_{\|\mathbf{r}''(t)\|^2} = \\ (x'(t)y''(t) - x''(t)y'(t))^2 + \underbrace{(x'(t)x''(t) + y'(t)y''(t))^2}_{\frac{1}{2} \frac{d}{dt} \{\|\mathbf{r}'(t)\|^2\}}$$

we find that the curvature defined by (11) satisfies the inequality  $\kappa(t) \leq \|\mathbf{r}''(t)\|/\|\mathbf{r}'(t)\|^2$ , with *equality* as soon as the velocity  $\|\mathbf{r}'(t)\|$  is constant.

Moreover, whenever  $\|\mathbf{r}''(t)\| \leq \gamma_0$  and  $\|\mathbf{r}'(t)\| \geq v_0$ , we have

$$\kappa(t) \leq \frac{\|\mathbf{r}''(t)\|}{\|\mathbf{r}'(t)\|^2} \leq \frac{\gamma_0}{v_0^2}.$$

## APPENDIX B PROOF OF THEOREM 2

*Proof:* We first evaluate the error between our model (samples along a piecewise linear trajectory) and the actual mobile sensor samples, within each segment. Then, we compute the Cramér-Rao lower bounds of the estimated 1D frequencies, in relation to this error, and assume that we are using a frequency estimation algorithm that reaches these bounds. Finally, relating the uncertainty on the trajectory to the uncertainty on the 1D frequencies through the condition number of a matrix that characterizes how distinct the spatial frequencies of the image are, we obtain the final expression.

### 1) Model inaccuracy

The uncertainty on the mobile sensor samples results from the error  $\sigma_{\text{lin}}$  caused by approximating a curve by line segments, and from the random error that corrupts the sensor measurements which we modelise as additive, white, Gaussian, with variance  $\sigma_{\text{noise}}^2$ . More specifically, since  $\|\mathbf{r}''(t)\| \leq \gamma_0$ , after double integration we find that the largest Euclidian distance between a curve  $\mathbf{r}(t)$  and its best piecewise-linear approximation  $\mathbf{r}_{\text{lin}}(t)$  is upper bounded as

$$\|\mathbf{r}(t) - \mathbf{r}_{\text{lin}}(t)\| \leq \|\mathbf{r}(t) - \mathbf{r}(t_0) - (t - t_0)\mathbf{r}'(t_0)\| \\ \leq \gamma_0 \frac{(t - t_0)^2}{2} \leq \frac{\gamma_0 N^2 T^2}{8}, \quad (12)$$

where  $t_0$  is the curve parameter corresponding to the middle point of a line segment and  $t$  is the parameter of any point within the same segment (hence,  $|t - t_0| \leq NT/2$ ). Here,  $T$  denotes the sampling step and  $N$  the number of samples within each segment.

Then, the noise-averaged mean-square difference between the actual samples,  $I(\mathbf{r}(t)) + \text{noise}$ , and the modeled samples,  $I(\mathbf{r}_{\text{lin}}(t))$ , can be upper bounded as follows:

$$\begin{aligned} \sigma_{\text{lin}}^2 &\stackrel{\text{def}}{=} \sigma_{\text{noise}}^2 + \frac{1}{NT} \int_{|t-t_0| \leq NT/2} |I(\mathbf{r}(t)) - I(\mathbf{r}_{\text{lin}}(t))|^2 dt \\ &\leq \sigma_{\text{noise}}^2 + \max_{|t-t_0| \leq NT/2} \|\mathbf{r}(t) - \mathbf{r}_{\text{lin}}(t)\|^2 \\ &\quad \times \max_{\mathbf{r}} \|\nabla I(\mathbf{r})\|^2 \\ &\leq \sigma_{\text{noise}}^2 + \frac{\gamma_0^2 N^4 T^4}{64} \max_{\mathbf{r}} \|\nabla I(\mathbf{r})\|^2 \\ &\leq \sigma_{\text{noise}}^2 + \frac{\gamma_0^2 N^4 T^4}{64} \underbrace{[b] \sum_k |c_k|^2}_{\mathcal{E}\{|I|^2\}} \underbrace{[b] \sum_k \|\mathbf{u}_k\|^2}_{1.2em \|\mathbf{U}\|_{\text{F}}^2}, \end{aligned}$$

where we have used that  $\nabla I(\mathbf{r}) = \sum_k j c_k \mathbf{u}_k e^{j \mathbf{u}_k^T \mathbf{r}}$  and Cauchy-Schwarz inequality. The above result is summarized by  $\sigma_{\text{lin}} \leq \sigma$  if we denote

$$\sigma \stackrel{\text{def}}{=} \sqrt{\mathcal{E}\{|I|^2\} \|\mathbf{U}\|_{\text{F}}^2 N^4 T^4 \gamma_0^2 / 64 + \sigma_{\text{noise}}^2}, \quad (13)$$

In what follows, we reinterpret  $\sigma_{\text{lin}}$  as the standard deviation of an additive Gaussian noise describing the uncertainty caused by the noise and the piecewise-linear model inaccuracy.

## 2) Cramér-Rao lower bounds of the 1D frequencies

We consider the uncertainties on the estimated 1D frequencies and amplitudes resulting from the uncertainty on the samples. To this end, we compute the Cramér-Rao lower bound of a frequency estimation problem, under additive white Gaussian noise of variance  $\sigma_{\text{lin}}^2$ . We have observed in [23] (see also [24], [32], [33]) that it is sufficient to consider the Cramér-Rao bound for individual frequencies since the other frequencies influence only mildly this calculation when they are sufficiently far apart. If  $\text{std}\{\omega\}$  designates the standard deviation of the error of estimating a 1D frequency  $\omega$ , associated with an amplitude  $c$ , the Cramér-Rao lower bound reads  $\text{std}\{\omega\} \geq 2\sqrt{3}N^{-3/2}T^{-1}\sigma_{\text{lin}}/|c|$ . It is known that the accuracy of algorithms like the maximum likelihood estimator (MLE) reach Cramér-Rao lower-bound empirically for a large range of noise variances and asymptotically, when the number of samples,  $N$ , tends to infinity [24]. This means that, if such efficient algorithms are used and  $N$  is large enough, this inequality is, for all practical purposes, an equality:

$$\text{std}\{\omega_k\} = \frac{2\sqrt{3}\sigma_{\text{lin}}}{TN^{3/2}|c_k|}, \quad (14)$$

for all frequency indices  $k$ , denoting by  $|c_k|$  the modulus of the amplitude of the sinusoid of 1D frequency  $\omega_k$ , which is also that of the 2D sinusoid of spatial frequency  $\mathbf{u}_k$  according to (4).

## 3) Trajectory uncertainty

The information conveyed by the frequency  $\omega_k$  is the scalar product between the slope of the piecewise-linear trajectory,  $\mathbf{r}'_{\text{lin}}(t)$ , which is constant within the chosen segment and the 2D spatial frequency,  $\mathbf{u}_k$ , of the image:  $\omega_k = \mathbf{u}_k^T \mathbf{r}'_{\text{lin}}(t)$ . In order to estimate  $\mathbf{r}'_{\text{lin}}(t)$ , we only need two independent scalar products  $\mathbf{u}_k^T \mathbf{r}'_{\text{lin}}(t) = \omega_k$ , for instance  $\omega_{k_1}$  and  $\omega_{k_2}$ . In that case, the error  $\Delta \mathbf{r}'_{\text{lin}}(t)$  on the slope satisfies the equation

$$\underbrace{\begin{bmatrix} \mathbf{u}_{k_1}^T \\ \mathbf{u}_{k_2}^T \end{bmatrix}}_{\mathbf{U}_{k_1,k_2}} \Delta \mathbf{r}'_{\text{lin}}(t) = \underbrace{\begin{bmatrix} \Delta \omega_{k_1} \\ \Delta \omega_{k_2} \end{bmatrix}}_{\Delta \omega_{k_1,k_2}},$$

which shows that  $\text{std}\{\mathbf{r}'_{\text{lin}}(t)\} \leq \text{std}\{\Delta \omega_{k_1,k_2}\}/\lambda_{k_1,k_2}$  where  $\lambda_{k_1,k_2}$  is the smallest singular value of  $\mathbf{U}_{k_1,k_2}$ . Now, using (14) we get that, for all  $k_1, k_2 \in \{1 \dots K\}$ ,

$$\begin{aligned} \text{std}\{\mathbf{r}'_{\text{lin}}(t)\} &\leq \frac{2\sqrt{3}\sigma_{\text{lin}}}{TN^{3/2}} \cdot \frac{1}{\lambda_{k_1,k_2}} \sqrt{\frac{1}{|c_{k_1}|^2} + \frac{1}{|c_{k_2}|^2}}, \\ &\leq \frac{2\sqrt{3}\sigma_{\text{lin}}}{TN^{3/2}} \cdot \underbrace{\min_{k_1,k_2} \left\{ \frac{1}{\lambda_{k_1,k_2}} \sqrt{\frac{1}{|c_{k_1}|^2} + \frac{1}{|c_{k_2}|^2}} \right\}}_{\text{def cond}\{\mathbf{I}\}} \end{aligned}$$

Then, integrating the uncertainties over all the samples (using the triangular inequality), the uncertainty on the reconstruction of the piecewise linear trajectory ( $L$  segments with  $N$  samples each) is upper bounded as

$$\text{std}\{\mathbf{r}_{\text{lin}}(t)\} \leq \frac{2\sqrt{3}L\sigma_{\text{lin}}}{\sqrt{N}} \text{cond}\{\mathbf{I}\}$$

Finally, adding the inaccuracy of the piecewise linear model (12), and taking into account the inequality  $\sigma_{\text{lin}} \leq \sigma$ , the total uncertainty on the ground-truth trajectory becomes

$$\text{std}\{\mathbf{r}(t)\} \leq \frac{2\sqrt{3}L\sigma}{\sqrt{N}} \text{cond}\{\mathbf{I}\} + \frac{\gamma_0 N^2 T^2}{8},$$

where  $\sigma$  is given by (13). ■

## REFERENCES

- [1] L. A. Treinish, *Visual Data Fusion for Applications of High-Resolution Numerical Weather Prediction*. Piscataway, NJ, USA: IEEE, 2000.
- [2] D. Fay and J. V. Ringwood, "On the influence of weather forecast errors in short-term load forecasting models," *IEEE Trans. Power Syst.*, vol. 25, no. 3, pp. 1751–1758, Aug. 2010.
- [3] B. Ducourthial, V. Cherfaoui, and T. Denoeux, "Self-stabilizing distributed data fusion," in *Proc. Symp. Self-Stabilizing Syst.*, 2012, pp. 148–162.
- [4] M. L. Yin and R. Arellano, "A risk analysis framework on GPS user range accuracy," in *Proc. Annu. Rel. Maintainability Symp.*, Jan. 2012, pp. 1–6.
- [5] H. P. Tan, Z. A. Eu, and W. K. G. Seah, "An enhanced underwater positioning system to support deepwater installations," in *Proc. OCEANS*, Oct. 2009, pp. 1–8.

- [6] S. Ehsan *et al.*, “Design and analysis of delay-tolerant sensor networks for monitoring and tracking free-roaming animals,” *IEEE Trans. Wireless Commun.*, vol. 11, no. 3, pp. 1220–1227, Mar. 2012.
- [7] N. Patwari, A. O. Hero, M. Perkins, N. S. Correal, and R. J. O’dea, “Relative location estimation in wireless sensor networks,” *IEEE Trans. Signal Process.*, vol. 51, no. 8, pp. 2137–2148, Aug. 2003.
- [8] N. B. Priyantha, H. Balakrishnan, E. D. Demaine, and S. Teller, “Mobile-assisted localization in wireless sensor networks,” in *Proc. IEEE 24th Annu. Joint Conf. IEEE Comput. Commun. Soc.*, 2005, vol. 1, pp. 172–183.
- [9] K. Lorincz and M. Welsh, “MoteTrack: A robust, decentralized approach to RF-based location tracking,” in *Proc. Int. Symp. Location-and Context-Awareness*, 2005, pp. 63–82.
- [10] H. Lee, M. Wicke, B. Kusy, and L. Guibas, “Localization of mobile users using trajectory matching,” in *Proc. 1st ACM Int. Workshop Mobile Entity Localization Tracking GPS-less Environ.*, 2008, pp. 123–128.
- [11] A. Thiagarajan, L. S. Ravindranath, H. Balakrishnan, S. Madden, and L. Girod, “Accurate, low-energy trajectory mapping for mobile devices,” in *Proc. 8th USENIX Conf. Netw. Syst. Des. Implement.*, Boston, MA, USA, 2011, pp. 267–280.
- [12] C. H. Tong, T. D. Barfoot, and É. Dupuis, “Three-dimensional SLAM for mapping planetary work site environments,” *J. Field Robot.*, vol. 29, no. 3, pp. 381–412, 2012.
- [13] A. Nuchter, H. Surmann, K. Lingemann, J. Hertzberg, and S. Thrun, “6D SLAM with an application in autonomous mine mapping,” in *Proc. IEEE Int. Conf. Robot. Autom.*, 2004, vol. 2, pp. 1998–2003.
- [14] R. Guo and T. Blu, “FRI sensing: Sampling images along unknown curves,” in *Proc. ICASSP IEEE Int. Conf. Acoust., Speech, Signal Process.*, May 2019, pp. 5132–5136.
- [15] I. Dokmanić, R. Parhizkar, A. Walther, Y. Lu, and M. Vetterli, “Acoustic echoes reveal room shape,” in *Proc. Nat. Acad. Sci.*, vol. 110, no. 30, pp. 12 186–12 191, 2013.
- [16] I. Dokmanić, R. Parhizkar, J. Ranieri, and M. Vetterli, “Euclidean distance matrices: Essential theory, algorithms, and applications,” *IEEE Signal Process. Mag.*, vol. 32, no. 6, pp. 12–30, Nov. 2015.
- [17] J. Murray-Bruce and P. L. Dragotti, “A sampling framework for solving physics-driven inverse source problems,” *IEEE Trans. Signal Process.*, vol. 65, no. 24, pp. 6365–6380, Dec. 2017.
- [18] T. Bailey and H. Durrant-Whyte, “Simultaneous localization and mapping (SLAM): Part II,” *IEEE Robot. Autom. Mag.*, vol. 13, no. 3, pp. 108–117, Sep. 2006.
- [19] A. Kim and R. M. Eustice, “Perception-driven navigation: Active visual SLAM for robotic area coverage,” in *Proc. IEEE Int. Conf. Robot. Autom.*, 2013, pp. 3196–3203.
- [20] V. Nguyen, A. Harati, A. Martinelli, R. Siegwart, and N. Tomatis, “Orthogonal SLAM: A step toward lightweight indoor autonomous navigation,” in *Proc. IEEE/RSJ Int. Conf. Intell. Robots Syst.*, 2006, pp. 5007–5012.
- [21] J. Heinrich, M. Burch, and S. I. O’Donoghue, “On the use of 1D, 2D, and 3D visualisation for molecular graphics,” in *Proc. IEEE Vis. Int. Workshop 3dvis*, 2014, pp. 55–60.
- [22] Z. J. Zheng and C. H. Leung, “Visualising global behaviour of 1D cellular automata image sequences in 2D maps,” *Physica A: Statist. Mech. Appl.*, vol. 233, no. 3-4, pp. 785–800, 1996.
- [23] T. Blu, P. Dragotti, M. Vetterli, P. Marziliano, and L. Coulot, “Sparse sampling of signal innovations,” *IEEE Signal Process. Mag.*, vol. 25, no. 2, pp. 31–40, Mar. 2008.
- [24] P. Stoica and A. Nehorai, “MUSIC, maximum likelihood, and Cramer-Rao bound,” *IEEE Trans. Acoust., Speech, Signal Process.*, vol. 37, no. 5, pp. 720–741, May 1989.
- [25] T. K. Sarkar and O. Pereira, “Using the matrix pencil method to estimate the parameters of a sum of complex exponentials,” *IEEE Antennas Propag. Mag.*, vol. 37, no. 1, pp. 48–55, Feb. 1995.
- [26] J. A. Cadzow, “Signal enhancement—A composite property mapping algorithm,” *IEEE Trans. Acoust., Speech, Signal Process.*, vol. 36, no. 1, pp. 49–62, Jan. 1988.
- [27] S. M. Kay, *Modern Spectral Estimation: Theory and Application*. Englewood Cliffs, NJ, USA: Prentice Hall, 1988.
- [28] V. F. Pisarenko, “The retrieval of harmonics from a covariance function,” *Geophysical J. Int.*, vol. 33, no. 3, pp. 347–366, 1973.
- [29] C. Gilliam and T. Blu, “Fitting instead of annihilation: Improved recovery of noisy FRI signals,” in *Proc. IEEE Int. Conf. Acoust., Speech, Signal Process.*, May 2014, pp. 51–55.
- [30] H. Pan, T. Blu, and M. Vetterli, “Towards generalized FRI sampling with an application to source resolution in radioastronomy,” *IEEE Trans. Signal Process.*, vol. 65, no. 4, pp. 821–835, Feb. 2017.
- [31] C. Gilliam and T. Blu, “Finding the minimum rate of innovation in the presence of noise,” in *Proc. IEEE Int. Conf. Acoust., Speech, Signal Process.*, Mar. 2016, pp. 4019–4023.
- [32] S. M. Kay and S. L. Marple, “Spectrum analysis—a modern perspective,” *Proc. IEEE*, vol. 69, no. 11, pp. 1380–1419, Nov. 1981.
- [33] B. Porat and B. Friedlander, “Computation of the exact information matrix of Gaussian time series with stationary random components,” *IEEE Trans. Acoust., Speech, Signal Process.*, vol. 34, no. 1, pp. 118–130, Feb. 1986.



**Ruiming Guo** received the B.E. degree in electronic engineering from Sichuan University, Chengdu, China, in 2017. He is currently working toward the Ph.D. degree with the Department of Electronic Engineering, The Chinese University of Hong Kong, Hong Kong. His research interests include sampling theory and image and signal processing.



**Thierry Blu** (Fellow, IEEE) was born in Orléans, France, in 1964. He received the “Diplôme d’ingénieur” degrees from the École Polytechnique, Palaiseau, France, in 1986, and Télécom Paris (ENST), France, in 1988, and the Ph.D. degree in electrical engineering from ENST, Paris, France, for a study on iterated rational filterbanks, applied to wideband audio coding, in 1996.

He was with the Biomedical Imaging Group, Swiss Federal Institute of Technology, Lausanne, Switzerland, from 1998 and 2007. He is currently a Professor

with the Department of Electronic Engineering, The Chinese University of Hong Kong, Hong Kong. His research interests include wavelets, approximation and sampling theory, sparse representations, image denoising, biomedical imaging, optics, and wave propagation.

Dr. Blu was a member of the IEEE Signal Processing Theory and Methods Technical Committee (2008–2013) and an Associate Editor for the IEEE TRANSACTIONS ON IMAGE PROCESSING (2002–2006), the IEEE TRANSACTIONS ON SIGNAL PROCESSING (2006–2010), and Elsevier’s *Signal Processing* (2008–2011). He is currently on the board of *EURASIP Journal on Image and Video Processing*, *SIAM Journal on Imaging Sciences*, and a member of the IEEE Bio Imaging and Signal Processing Technical Committee. He was the recipient of two best paper awards from the IEEE Signal Processing Society (2003 and 2006). He is also the coauthor of a paper that received a Young Author Best Paper Award (2009) from the same society.